Calculation of initial stage of solidified shell deformation during γ to δ transformation in mold.

Kohei Furumai[1], Hatem S. Zurob[2] and A.B.Phillion[2].

(1) Steelmaking Research Department, Steel Research Laboratory, JFE Steel Corporation,

1 Kokan-cho, Fukuyama, Hiroshima, Japan, 721-8510

(2) Department of Materials Science and Engineering, McMaster University, 1280 Main St West,

Hamilton, ON, Canada, L8S 4L7

Abstract

Solidification shell deformations within the mold during continuous casting have been calculated in order to clarify the influence of mold flux infiltration variability on the cooling rate, the width of the low heat flux region, the height of the air gap, the unevenness of the solidified shell, and the resulting strain in the solidified shell. A sequentially coupled thermal-mechanical finite element model has been developed to perform the calculations. The simulation includes heat transfer and shell deformation in a growing solidified shell, along with the delta-to-gamma transformation. Further, it takes into account the effects of variability in mold flux infiltration and air gap formation on heat transfer into the mold, as well as the effect of cooling rate on the thermal expansion resulting from delta-to-gamma transformation. The results show that mild cooling and a small region of low heat flux (i.e. low variability in mold flux infiltration) strongly decrease the height of the air gap, the unevenness in the solidified shell and the strain in the solidified shell. It is confirmed that it is important to optimize the cooling rate and prevent the variation in mold flux infiltration, especially near region of δ to γ transformation, in order to minimize longitudinal crack formation.

Keywords: continuous casting; delta to gamma transformation; air gap; hypo-peritectic steel; uneven mold flux infiltration; uneven solidification; longitudinal crack

1. Introduction

Surface cracking is a particularly serious problem during continuous casting. In recent years, high throughput conditions have been required to improve surface quality and overall productivity.[1] However, higher casting velocities have also led to an increase in longitudinal crack formation, especially in hypo-peritectic grades. These defects form due to a set of factors, namely (1) unevenness in the solidified shell thickness occurring with higher casting velocities and (2) solidified shell deflection occurring during δ to γ transformation as a result of a large change in thermal expansion coefficient.[2-8] It is thought that these two factors are related. Prior simulations of shell deflection during δ to γ transformation have shown that the air gap and thus the solidified shell can become uneven because of variations in γ formation.[9-10] Further, within

the mold, local variations in the cooling rate of the solidified shell can affect its unevenness.[5,11]

One of the primary uses of mold flux is to prevent uneven solidification and longitudinal cracking by stabilizing and enhancing heat transfer between the solidified shell and the mold.[12-14] However, uneven mold flux infiltration can result in severe uneven solidification.[15] At present, simulations of heat transfer in the mold have focused on comparing differences between mold fluxes, but not the effects of process-driven variations nor material property variations. It is these variations that lead to longitudinal cracks. In this study, the effect of mold flux on the deformation of the solidified shell and its unevenness are investigated. Two mold fluxes, representative of high and low heat transfer conditions, are evaluated via Finite Element Analysis for their performance in terms of the height of the air gap, shell unevenness and shell strain during the initial stages of transit through the mold. The occurrence of uneven mold flux infiltration is modeled by adding a low heat flux region within the domain. The cooling-rate-dependent γ phase evolution is taken into account through the thermal expansion coefficient.

2. Mathematical Model

2.1.Thermo-mechanical simulation

The 2D heat transfer and shell deformation analysis of a Fe-0.1wt%C hypo-peritectic steel during solidification within the mold was carried out with using the commercial FE package ABAQUS. The geometries of the thermal and stress models are shown in Fig. 1. The thermal model, Fig. 1(a), consists of a quarter cross-section of a slab 250 mm in thickness and 1000 mm in width that contains both liquid and solid steel. The deformation model, Fig. 1(b), consists of a half-section of the solidified shell along the wide face. A flowchart of the simulation procedure is shown in Fig.2. First, the thermal simulation is initiated to extract heat from the surface of the solidified shell. As can be seen in Fig. 1(a), different heat flux values are applied to different regions of the wide face at y=0 to represent uneven mold flux infiltration. The surfaces x=0 mm and y = 125 mm are symmetry planes and thus adiabatic. The surface at x = 500 mm represents the narrow face of the slab, and for simplicity is neglected. The uneven mold flux infiltration on the wide face will result in thinning in some sections of the solidifying shell. Second, the solid shell is meshed and the deformation calculation carried out. Deformation is induced by thermal contraction during the δ to γ transformation. The transformation, and thus thermal contraction will vary between the different regions because the different cooling rates will accelerate/ retard γ formation. The resulting equilibrium creates an air gap that further retards heat transfer thus further thins the shell and increases the size of the air gap [11]. These two models are coupled sequentially, with a time-step of 0.1 s and an element size of 0.2 mm. Specifically, at each time step the solid shell geometry, i.e. all elements having $T < T_s$, is passed from the thermal model

to the deformation model while the height of the air gap (resulting in further loss in heat flux) is passed from the deformation model to the thermal model. Re-meshing of the solid shell occurs at each time-step. The re-meshed elements contained the strain accumulated from the previous time-step. Example solid geometries at t=0 s, 0.1 s and 0.2 s are shown in Fig. 1(b). A casting speed of 1.5 m/min is used for all calculations, covering the first 10 s of the casting process.

The thermal model solves the heat transfer equation, with a heat flux boundary condition, i.e.

$$C\rho\frac{dT}{dt} = \frac{\partial}{\partial x}\left(k\frac{\partial T}{\partial x}\right) + \frac{\partial}{\partial y}\left(k\frac{\partial T}{\partial y}\right) \quad (1)$$

$$-k\frac{\partial T}{\partial n} = q(t) \quad (2)$$

where C is the heat capacity [0.68 kJ/kg/K] [16], ρ is the density [kg/m^3], k is the thermal conductivity [15.9+0.01151T W/m/K][16], T is the temperature [K], t is time [s], x and y are the distances along the width direction in the mold [m], and the distance from the strand surface [m], n is an outward-facing normal to the slab surface and $q(t)$ is the time-dependent heat flux on the slab surface [W/m^2]. The latent heat (ΔH [272.1 J/g][17]) effect is applied by increasing the heat capacity term between liquidus (T_L) and solidus (T_s) temperatures. T_L and T_S were calculated using the TCFE6 database of THERMOCALC.[18] The initial temperature of the liquid steel was set to T_L +10K.

The heat flux profiles measured by Knazawa et al.[6] were used as input values in the present study to simulate casting. Knazawa measured the heat flux occurring when using different mold fluxes at a position 45 mm below the meniscus for a range of casting speeds up to 5.0 m/min. In this present study, the measurements for two mold fluxes (high and low heat flux, denoted A and B) expressed by casting speed were converted to heat flux profiles expressed by transit time from the meniscus. The transit time t_T is given as the ratio of the distance from the meniscus to the measurement thermocouple (45 mm) and the casting speed. The discrete points were then fit to exponential-type equations for data extrapolation.[19]-[20]. Fig. 3 shows the resulting heat flux for mold fluxes A, qMF-A, and B, qMF-B.

qMF-A and qMF-B provide the variation in heat flux with time as the slab moves through the mold. In addition, the heat flux will vary spatially because of uneven mold flux infiltration. To account for this variation, the wide face surface is divided into three regions[10] – a low heat flux region at the center of the slab (R1, $0 < x < a$), a shell deflection region (R2, $a \leq x \leq b$) and a normal region (R3, $x > b$) – as shown in Fig. 1. The low heat flux region is placed at the center because that is where longitudinal cracks generally occur. This low heat flux region will result in a local solidification delay, leading to unevenness of the solidified shell. Following, Terauchi and

3

Nakata, who observed heat flux variations in the width direction near the meniscus of ~20%,[21] it is assumed initially ($t=0$) that the heat flux in R1 has a value of 80% as compared to the measured value used in R3. In R2, the heat flux will be initially set to equal the heat flux in R3. The heat flux in both R1 and R2 will then decrease during the process because of the formation of the air gap.

The concept of thermal resistivity, shown schematically in Fig. 4, is used to account for the variation in heat flux in R1 and in R2 resulting from the formation of the air gap as well as the thinning of the solidified shell. At $t>0$, heat flux in the three regions is given by[22]

$$q_1(t) = \frac{(T_s - T_W)}{R_1(t) + \Delta R_1(t)} \quad (3)$$

$$q_2(t) = \frac{(T_s - T_W)}{R_2(t) + \Delta R_2(t)} \quad (4)$$

$$q_3(t) = q_{MF-A}(t) \text{ or } q_{MF-B}(t) \quad (5)$$

where $q_1, q_2,$ and q_3 are the heat fluxes in R1, R2, and R3 [W/m^2], T_w is temperature of water in the mold [298 K], R_1 and R_2 are the baseline thermal resistivities of R1 and R2 [m^{2}K/W], and ΔR_1 and ΔR_2 are its variation caused by the air gap and change in solidified shell thickness [m^{2}K/W]. The terms R_1 and R_2 contain contributions from the solidified shell, mold flux, and mold, as shown by

$$R_1(t) = \frac{(T_s - T_W)}{0.8 \cdot q_3(t)} = R_1(t)_{shell} + R_1(t)_{mold\,flux} + R_1(t)_{mold}, \quad (6)$$

$$R_2(t) = \frac{(T_s - T_W)}{q_3(t)} = R_2(t)_{shell} + R_2(t)_{mold\,flux} + R_2(t)_{mold} \quad (7)$$

Similarly, the variation in thermal resistance in the low heat flux and shell deflection regions are given by

$$\Delta R_1(t) = R_1(t)_{airgap} + (R'_1(t)_{shell} - R_1(t)_{shell}) \quad (8)$$
$$\Delta R_2(t) = R_2(t)_{airgap} + (R'_2(t)_{shell} - R_2(t)_{shell}) \quad (9)$$

where the terms $R'(t)_{shell}$ is the thermal resistivity of the solidified shell with an air gap [m^{2}K/W], and $R(t)_{air\,gap}$ is the thermal resistivity of the air gap [m^{2}K/W]. $R(t)_{air\,gap}$ is calculated from the air gap height at each node along R1 or R2 as d_t/λ_{airgap} where λ_{airgap} is the thermal conductivity of air. The values of $R_1(t)_{shell}$ and $R_2(t)_{shell}$ were determined by performing additional heat transfer simulations, without an air gap, as

$$R_1(t)_{shell} = \frac{(T_s - T(t)_{1,shell\,surface})}{0.8 \cdot q_3(t)} \quad (9a)$$

$$R_2(t)_{shell} = \frac{(T_s - T(t)_{2,shell\,surface})}{q_3(t)} \quad (9b)$$

The values of $R'_1(t)_{shell}$ and $R'_2(t)_{shell}$ were calculated in the same way but using the shell surface temperatures from the coupled model containing an air gap. An explicit method was used to determine the change in resistances with the values from one time-step projected to the next. It has been reported that the total width of shell deflections associated with the longitudinal cracks in low carbon steel can vary between 2-38mm. [24] In these simulations, the width of shell deflection, i.e. parameter *b* in Fig. 1, has been set to 2.5 mm. The width of the low flux region, i.e. parameter *a* in Fig. 1, is used as a parameter for investigation. Note also that it is assumed that qMF-A and qMF-B do not contain any thermal resistance contributions from the air gap, as there was no deflection of the solidified shell[10,11].

  The mechanical model requires geometry, boundary conditions and a constitutive law in order to simulate the air gap formation. Three instances of the geometry are shown in Fig. 1(b). As can be seen, over time the air gap becomes integrated within the geometry, and the solidified shell thickens but also becomes uneven. Boundary conditions are needed on all four sides of the domain: (1) A pressure *P* [Pa] is applied at the boundary between the liquid and the solidified shell corresponding to the ferrostatic pressure, $P = \rho g v_c t$, where g is the gravitational acceleration [m/s^2] and v_c is the casting speed [m/s]. (2) The nodes are constrained in *x* on the symmetry plane at *x*=0. (3) The nodes are free to move in *x* on the narrow face surface. (4) The nodes on R1 and R2 on the wide face surface are free to move while the nodes on R3 are constrained in *y* [10,11]. The elastic modulus measured from Mizukami et al[25] was employed. The Poisson's ratio was assumed to be 0.3. A rate dependent plasticity constitutive law was used to predict the temperature and strain-rate dependency on yield stress[26],

$$\dot{\varepsilon}_p = A exp\left(-Q/_{RT}\right) [sin\, h(\beta K)]^{1/m} \quad (10)$$

$$Y_0 = K\varepsilon_p^s \quad (11)$$

where A, β, and m are constants, R is the gas constant [J/K/mol], Q is the activation energy for deformation [J/mol], K is the strength coefficient, *n* is the strain hardening exponent, ε_p and $\dot{\varepsilon}_p$ are the effective plastic strain and plastic strain rate [1/s]. The values of A, β, s, Q and *m* in δ and γ are taken from the work of Han et al[27]. A rule of mixtures is used to calculate the yield stress of the γ/δ composite. Note that it is assumed that time evolution in ferrostatic pressure for qMF-B increases in the same manner as qMF-A, pushing the shell toward the mold and decreasing the height of air gap, even though the two mold fluxes will give different solidified shell evolutions.[11]

2.2.Delta to Gamma Transformation Model

  The evolution in γ during the δ to γ transformation was calculated to estimate the thermal expansion coefficient. The model employed is the one-dimensional model proposed by

Konishi et al[20]. The key assumptions of the model are a negligible undercooling below the peritectic temperature, carbon-diffusion control of the growth of γ phase, a domain size of a single grain of average grain size, uniform carbon concentration within the δ phase and local equilibrium at the δ/γ interface. In this model, carbon diffusion in the gamma phase is expressed by

$$\frac{\partial C_\gamma}{\partial t} = D_\gamma \frac{\partial^2 C_\gamma}{\partial x^2} \quad (12)$$

where C_γ is the carbon concentration in the gamma phase, and D_γ is the diffusion coefficient of carbon in γ [m²/s] [28]. The velocity of the moving δ/γ interface is expressed by

$$V = -\frac{D_\gamma}{\left(C_\gamma(T) - C_\delta(T)\right)} \left.\frac{\partial C_\gamma}{\partial x}\right|_{int} + V_\delta \quad (13)$$

where V is the velocity of the δ/γ interface [m/s], and $C_\gamma(T)$ is the equilibrium carbon concentration of the δ phase at the interface. The V_δ, i.e. the contribution to the velocity of the interface due to carbon diffusion in the delta phase, can be expressed as

$$V_\delta = -\frac{1-f_\gamma}{\left(C_\gamma(T) - C_\delta(T)\right)} \frac{\lambda}{2} \frac{dC_\delta(T)}{dT} \frac{dT}{dt} \quad (14)$$

where f_γ is the volume fraction of the gamma phase, and λ is the grain size [m]. The grain size is assumed to correspond to the primary dendrite-arm spacing. This can be linked to the cooling rate as $\lambda = 352.5\dot{T}^{-0.39}$ where λ and CR are given in [µm] and [K/s] [29].

Examples of the calculated volume fraction of γ as a function of temperature are shown in Fig. 5 (a). As can be seen, the transformation become significantly retarded with increased cooling rate. The thermal expansion coefficient, corresponding to the linear shrinkage of the solidified shell, can be determined from these calculations as

$$\alpha(t) = \alpha_\gamma(T) \cdot f_\gamma(t) + \alpha_\delta(T) \cdot (1 - f_\delta(t)) \quad (15)$$

where $\alpha_\gamma(T)$ and $\alpha_\delta(T)$ are the temperature-dependent thermal expansion coefficients of γ and δ at T. The resulting linear shrinkage is shown in Fig. 5 (b) employing the temperature-dependent lattice parameter equations in δ-steel and γ-steel reported by Chandra et al.[19,30] Thus, cooling rates are seen to have small but measurable effects on the coefficient of thermal expansion. These effects will lead to the formation of an air gap during continuous casting. Note that within the Abaqus simulation, the reference temperature for thermal expansion was set to the peritectic transformation temperature.

3. Results and Discussion

Fig. 6 shows the contour plots of solidified shell displacements calculated using the coupled thermo-mechanical analysis for both q$_{MF-A}$ and q$_{MF-B}$ after 1 mm of solidified shell

thickness has formed in R3. For this set of simulations, the width of R1, *i.e.* parameter *a*, was set to 0.7 mm. As can be seen, an air gap has formed in both cases beginning at the edge of the shell deflection region (x=*b*) and increasing inward towards the low heat flow region (R1). The largest air gap is at the centerline, as excepted given the applied boundary conditions. Comparing the two simulations, it can be seen that the mild cooling of q$_{MF-B}$ in R3 significantly reduces by nearly fifty percent the height of the formed air gap. The small cooling-rate conditions lessen the difference in austenite formation between R3 and R1 and thus lessen the difference in thermal contraction in the different zones.

The unevenness in the solidified shell, σ, can be defined as [10]

$$\sigma = \frac{d_1 - d_2}{d_1} \cdot 100 \quad (16)$$

where d_1 and d_2 are the shell thicknesses within R3 (at *x*=2*b*) and R1 (at *x*=0), respectively. The maximum air gap height (h_{ag}^{max})) and solidified shell unevenness (σ) are plotted in Fig. 7 as a function of d_1 for both mold fluxes. As can be seen, h_{ag}^{max} and σ both increase at the beginning of casting, just below the meniscus, but then decrease after a maximum value is reached. The maximum in unevenness is significant as there is nearly a 65% difference between the two mold fluxes. Further, there are strong differences in shell thickness between R3 and R1 making the low heat flux region quite susceptible to cracking. For the case using q$_{MF-B}$ as mold flux, h_{ag}^{max} and σ are lower during the slab's transit through the mold, while the rate of air gap decrease after the peak is higher than that of q$_{MF-A}$. Fig. 8 shows the corresponding heat flux within R1 (at *x*=0) and R3 during the simulations used to generate Fig. 7 as a function of d_1. As can be seen, the air gap has a strong effect on heat flux. For q$_{MF-A}$, with a large air gap there is a large difference between the heat flux in R1 and in R3 whereas for q$_{MF-B}$ the difference is not so great. Since a 20% reduction in heat flux in R1 was imposed, to account for variations in mold infiltration, it would appear that the role of the air gap is small for q$_{MF-B}$ whereas it is significant for q$_{MF-A}$. As the solidified shell thickens, the curves approach each other as the air gap is diminished.

The effect of the air gap on heat transfer is further explored in Fig. 9, which shows the ratio of the thermal resistivity of the air gap (at *x*=0) to the overall thermal resistivity between the molten steel and the water (Fig. 4) as a function of d_1. For q$_{MF-A}$, the air gap resistivity accounts for nearly 60% of the total thermal resistance at its largest value, decreasing to 20% as the slab transitions through the mold. For q$_{MF-B}$, the air gap resistivity accounts for 40% of the total thermal resistance at its largest value, decreasing to less than 10% later on. The influence of the evolution in surface temperature of the solidified shell in R1 (at *x*=0) with mold flux A on the air gap formation is shown in Fig. 10. As can be seen, the surface temperature first decreases below the peritectic transformation temperature, then increases, then further decreases. These results

7

help to provide insight into the mechanism of air gap formation. Once the δ to γ transformation starts, the air gap forms thus decreasing the total heat flux that can be removed by the mold, and increasing the temperature near the surface of the solidified shell. Subsequently, the height of the air gap decreases which is related to the increase in ferrostatic pressure as the slab transitions through the mold away from the meniscus. It is clear from these results that the initial stage of δ to γ transformation is the critical physical parameter controlling air gap formation. Fig. 11 shows the measured unevenness of solidified shell[11,31] for a 0.12 wt.%C steel continuously cast at a velocity of 1.2m/min, and compared with the calculated result using mold flux A. As can be seen in the figure, the calculated result matches remarkably well against the experimental data, considering all the simulation uncertainties and assumptions. Both the calculated and measured results of unevenness of solidified shell σ decrease with time.

Fig. 12 examines the effects of Parameter a on (a) the profile of the air gap when the solidified shell in R3 is 1 mm in thickness, and (b) the unevenness in the solidified shell thickness for two different values of d_1. These calculations were conducted using q_{MF-A}. The results shown in both figures demonstrate that the width of the low heat flux region has a strong effect on air gap formation and shell unevenness, potentially leading to longitudinal crack formation. In (a), it can be seen that, while initially the parameter a strongly affects the air gap profile, the curves seem to reach a similar shape when a=0.7, 1.0 or 1.6 mm and for these three cases the maximum air gap heights are almost the same. This is an indication that, although the model contains strong assumptions, important insight into air gap formation can be obtained. In (b), it can be seen that the parameter a also significantly affects the unevenness in the solidified shell thickness, both near the meniscus at d_1=1 mm and further away at d_1=2 mm. Although the unevenness decreases with increasing distance, there is still high variability in σ because of the significant decrease in heat flux that occurs throughout the length of the mold when a is increased.

It is well known that the variations in mold flux infiltration along the wide face of the slab occur because of variation in mold flux, fluctuations in mold level and temperature, and flow behavior of the molten steel all affect the occurrence of a low heat flux region. The results from the new thermal-mechanical simulations demonstrate and reinforce the need to prevent fluctuation of the mold flux infiltration. These results are in good agreement with the results reported by Miyasaka et al[15] that longitudinal cracks occur with the large variation in the thickness of the mold flux film along the wide face of the mold. Techniques such as electromagnetic brake or electromagnetic stirring [32-33] are highly beneficial in this regard.

The main goal behind understanding air gap formation and solidified shell unevenness is to reduce longitudinal crack formation. The newly-developed model can be used in this regard. It is reported that longitudinal cracks initiate as hot tears near the solid-liquid interface due to the

strain caused by unevenness in the solidified shell and then propagate towards the surface of a slab.[10,11] Won et al. [34] developed a criteria to determine the critical strain for cracking near the solid-liquid interface that takes into account the brittle temperature range between the liquid impenetrable temperature (LIT) and zero ductility temperature (ZDT), as well as the applied strain rate, and the mechanical properties of the semisolid,

$$\varepsilon_c = \frac{\varphi}{\dot{\varepsilon}^{m^*} \Delta T_B^{n^*}} \quad (17)$$

$$\Delta T_B = LIT - ZDT = T(f_s = 0.9) - T(f_s = 0.99) \quad (18)$$

where ε_c is critical strain for the cracking, $\dot{\varepsilon}$ is the applied strain rate, φ, m^* and n^* are material properties linked to the sensitivity to cracking, ΔT_B is the brittle temperature range [˚C], and LIT and ZDT correspond to the temperatures at which the solid fractions become 0.9 and 0.99. Fig. 13 shows the ratio of the strain ε within R1 (at x=0) at the inner edge of the solidified shell (corresponding to the solid-liquid interface) calculated by the mechanical model to the critical strain ε_c for both q_{MF-A} and q_{MF-B} as a function of time. The material parameters proposed by Senk et al.[35] (φ=0.00427, m^*=0.4151 and n^*=0.9979) were employed to determine ε_c. The value of ΔT_B was calculated from the equilibrium phase diagram using THERMOCALC[18] based on a Fe-0.1 wt.%C alloy; this value is especially sensitive to composition.[35] As can be seen, the ratio of ε to ε_c reaches a maximum value for both mold fluxes, but then remains approximately constant with increasing d_1 for the case using q_{MF-A} whereas it decreases for the case using q_{MF-B}(t). The specific prediction is that a crack will form while using mold flux A since the ratio $\varepsilon/\varepsilon_c$ exceeds one, while it will not occur while using mold flux B. However, this is an arbitrary distinction since the calculation of ε_c depends strongly on alloy composition.[35] What is more significant is that the ratio decreases beyond the maximum with mild cooling in the mold whereas it remains at the maximum value for high mold cooling. This demonstrates the importance of controlling the cooling rate and mold flux infiltration, especially at the initial stage of solidification, to prevent the longitudinal cracks.

4. Conclusions

The effects of the cooling rate and the width of low heat flux region on the height of air gap, unevenness of solidified shell and strain of solidified shell at the initial stage of solidification in the mold have been studied on the basis of the developed delta-to-gamma transformation, heat transfer and solidified shell deformation calculations. It can take into account the effect of cooling rate on the thermal expansion coefficient used in the shell deformation calculation. The cooling rate and the width of low heat flux region significantly affect the unevenness of the solidified shell as well as the height of the air gap in the mold. In the case of mild cooling, the

height of the air gap reduced compared to the case of high cooling condition because of large ferrostatic pressure at the same solidified shell thickness. This effects is also explained by the ratio of strain to critical strain in the solidified shell. From these results, in order to prevent the air gap formation, unevenness of solidified shell, leading to longitudinal cracks, it is important to optimize the cooling rate and prevent the variation and width of mold flux infiltration along the width direction in the mold, especially at near the meniscus region δ to γ transformation.

Figures

Figure 1: Geometries used for FEA ((a) Thermal model, (b) Stress model). Note that x = 0 mm corresponds to the centerline

(a)   (b)
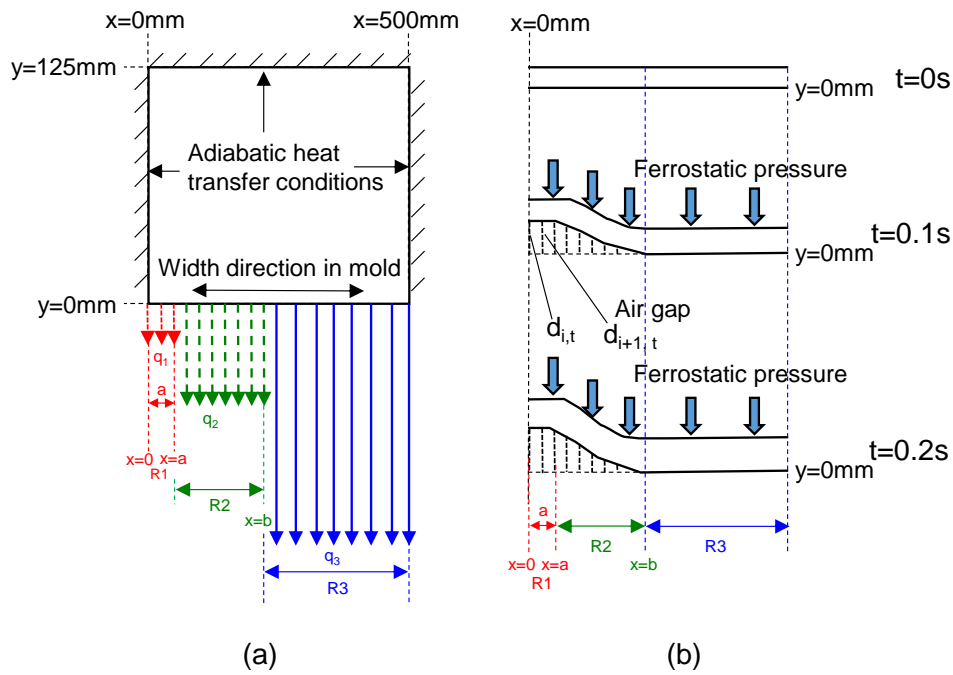
Figure 2: Flowchart of calculation procedure
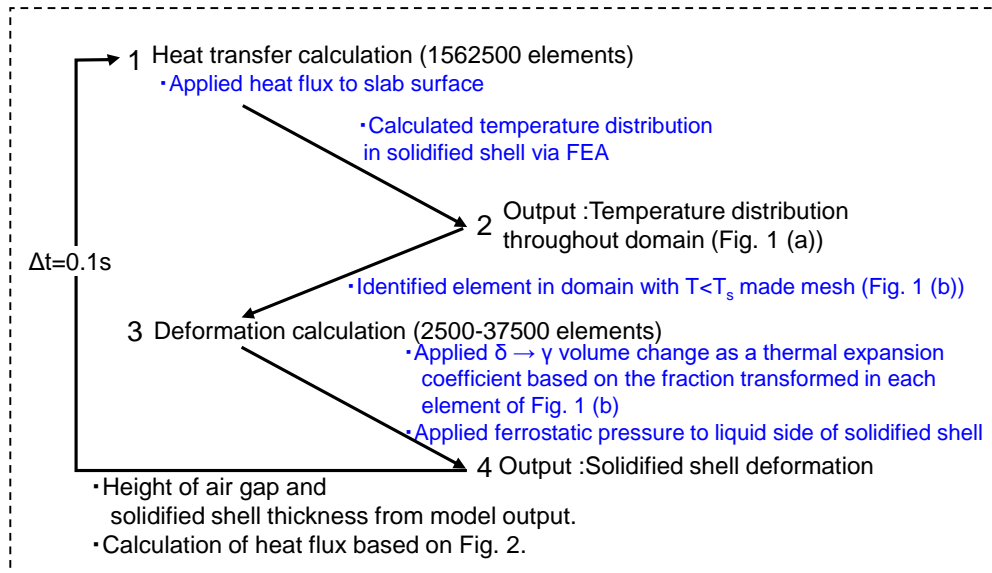
Figure 3: Variation in applied heat flux as a function of transit time from meniscus for mold flux A and mold flux B
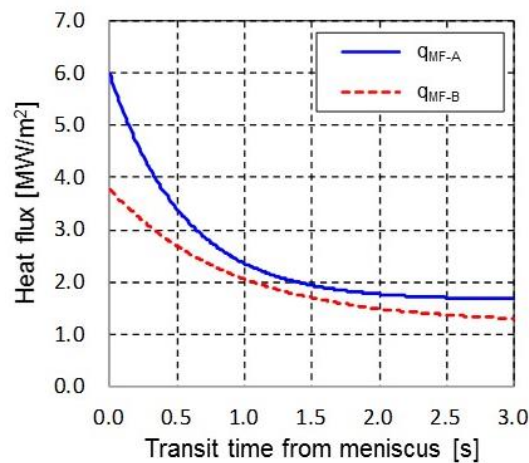
Figure 4: Schematic of heat flow between molten steel and cooling water
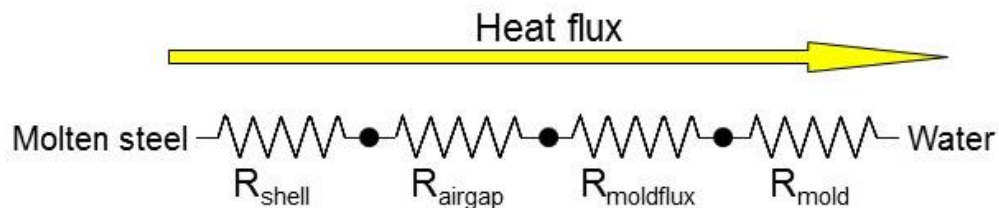
Figure 5: (a) Evolution in volume fraction of austenite and (b) Linear shrinkage of the solidified shell for different cooling rates
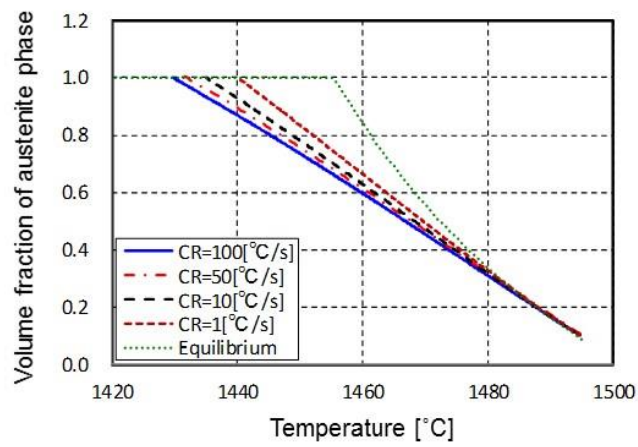
(a)
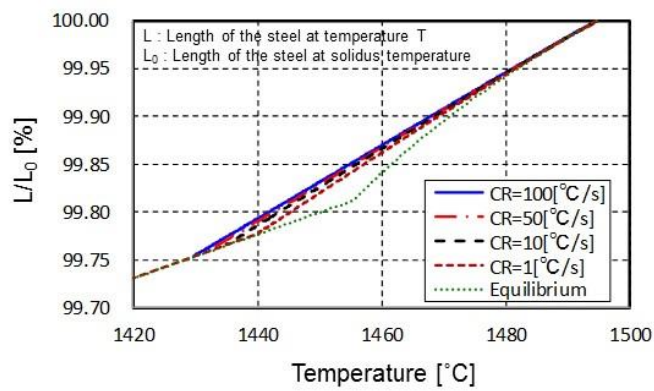
(b)

Figure 6: Contour plots of solidified shell displacement calculated by using (a) q_{MF-A} and (b) q_{MF-B} at 1 mm of shel thickness in R3. The deformation geometry has been magnified by 5 times. Parameter a = 0.7 mm

(a)

(b)
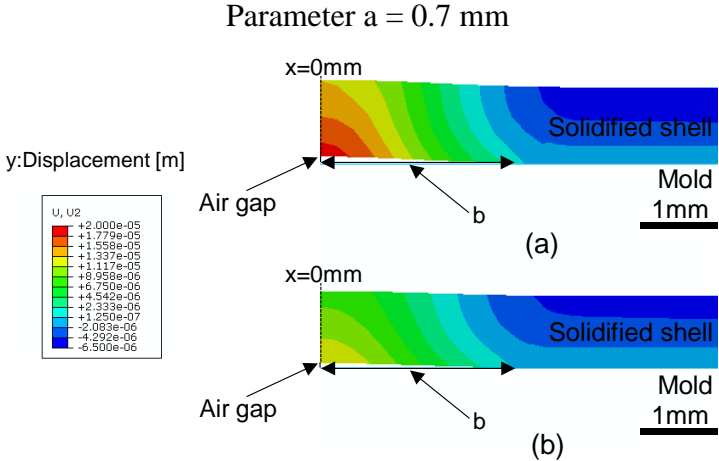
Figure 7: Maximum air gap height and unevenness of solidified shell as a function of shell thickness away from air gap. Parameter a = 0.7 mm
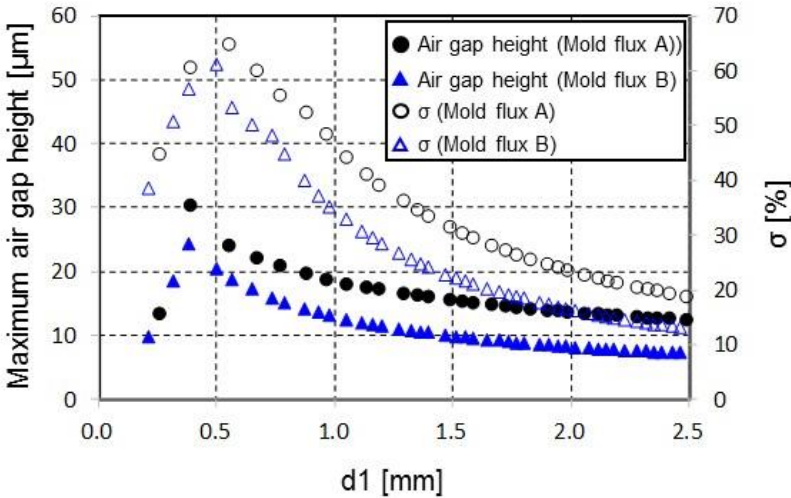
Figure 8: Heat flux within R1 (at x = 0) and R3 as a function of solidified shell thickness in R3 for both q_{MF-A} and q_{MF-B}. Parameter a = 0.7 mm
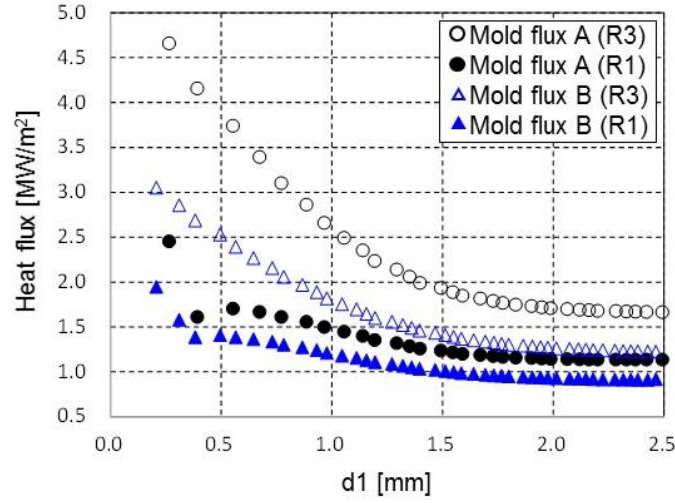
Figure 9: Ratio of thermal resistivity of air gap to total thermal resistivity in R1 (at x = 0) as a function of shell thickness in R3. Parameter a = 0.7
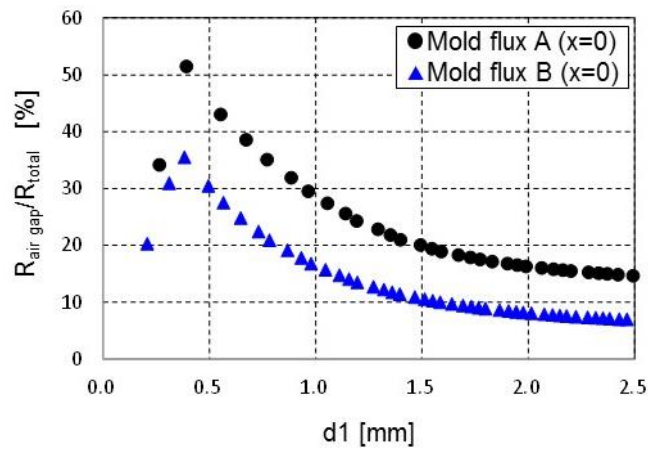
Figure 10: Influence of surface temperature of solidified shell at x = 0 on the air gap forming
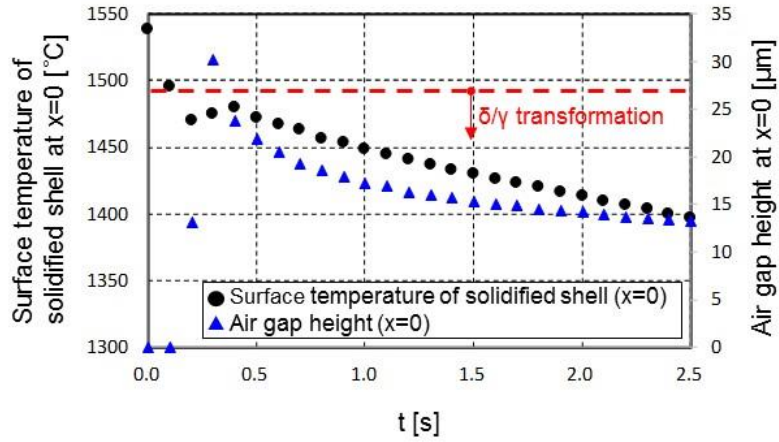
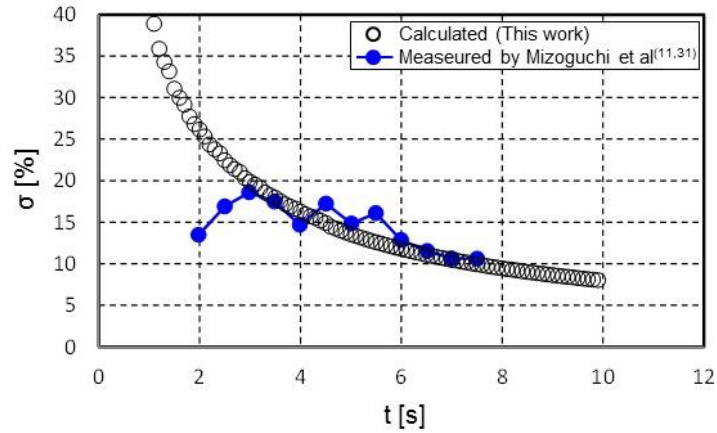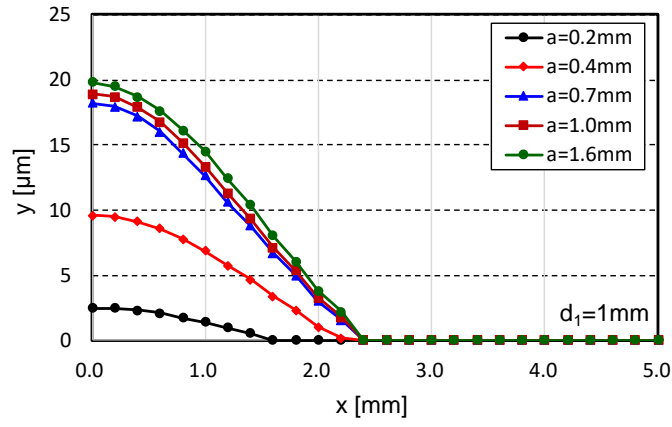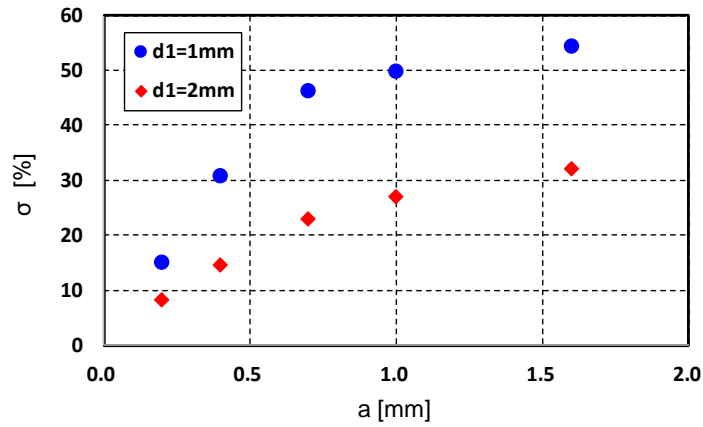Figure 11: Measured unevenness of solidified shell compared with the calculated result

Figure 12: Effect of Parameter *a* (width of low heat flux region) on (a) air gap profile and (b) unevenness in the solidified shell thickness
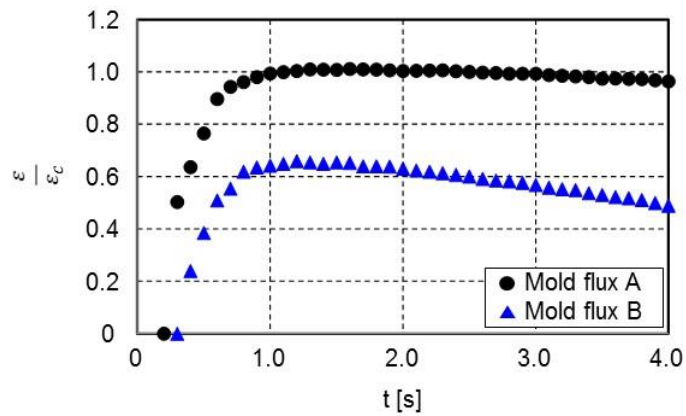
(a)

(b)

Figure 13: Ratio of the calculated evolution in strain ε to critical strain ε_c for the case of high and mild cooling. Parameter a $= 0.7$

References

1) M. S. Kulkarni and A. Subash Babu: *Journal of Materials Processing Technology*, 166

(2005), 294.

2) A. Grill and J. K. Brimacombe: *Ironmaking Steelmaking*., 3 (1976), 76.

3) T. Saeki, S. Ooguchi, S. Mizoguchi, T. Yamamot, H. Misumi and A. Tsuneoka: *Tetsu-to-Hagané*, 68 (1982), 1773.

4) Y. Sugitani, M. Nakamura and T. Watanabe: *Tetsu-to-Hagané*, 67 (1981), 1508.

5) H. Nakato, M. Ozawa, K. Kinoshita, Y. Habu and T. Emi: *Tetsu-to-Hagané*, 67 (1981), 1200.

6) T. Kanazawa, S. Hiraki, M. Kawamoto, K. Nakai, K. Hanazaki and T. Murakami: *Tetsu-to-Hagané*, 83 (1997), 701.

7) M. Suzuki and Y. Yamaoka: *Mater. Trans*., 44 (2003), 836.

8) M. Suzuki, M. Suzuki and M. Nakada: *ISIJ Intl*., 41 (2001), 670.

9) H. Murakami, M. Suzuki, T. Kitagawa and S. Miyahara: *Tetsu-to-Hagané*, 78 (1992), 105.

10) T. Matsumiya, T. Saeki, J. Tanaka and T. Ariyoshi: *Tetsu-to-Hagané*, 68 (1982), 1782.

11) T. Mizoguchi, S. Ogibayashi and T. Kajitani: *Tetsu-to-Hagané*, 81 (1995), 971.

12) K. Nakai, T. Sakashita, M. Hashio, M. Kawasaki, K. Nkajima and Y. Sugitani: *Tetsu-to-Hagané*, 73 (1987), 498.

13) J. A. Kromhout, E. R. Dekker, M. Kawamoto and R. Boom: *Ironmaking Steelmaking*., 40 (2013), 206

14) T. J. H. Billany, A. S. Normanton and P. Grieveson: *Ironmaking Steelmaking*., 18 (1991), 403.

15) N. Miyasaka, T. Hiraoka, O. Kitamura, T. Ono, S. Ando and T. Ohashi: *Tetsu-to-Hagané*, 78 (1978), S663.

16) I.G. Saucedo, J. Beech, and G.J. Davies: *Met. Technol*., 9 (1982), 282.

17) L.A. Baptista: Master's Thesis, The University of British Columbia, Vancouver, (1979).

18) Available from THERMO-CALC software, www.thermocalc.com.

19) J. Konishi: Master's Thesis, The University of British Columbia, Vancouver, (1996).

20) J. Konishi, M. Militzer, J.K. Brimacombe, and I.V. Samarasekera: *Metall. Mater. Trans.B*., 33 (2002), 413

21) M. Terauchi and H.Nakata: *5tn European Continuous Casting Conference, Nice, France*, 1 (2005), 28.

22) T. Odagaki, N. Aramaki amd Y. Miki: *Tetsu-to-Hagané*, 102 (2016), 560.

23) J. P. Holman: Heat Transfer, ed. by McGraw-Hill, Maruzen, Tokyo, (1982), 263.

24) J. K. Brimacombe, F. Weinberg and E. B. Hawbolt: *Metall. Mater. Trans.B*., 10 (1979), 279.

25) H. Mizukami, K. Murakami and Y. Miyashita: *Tetsu-to-Hagané*, 63 (1977), S562.

26) H. N. Han, Y. Lee, K. H. Oh and D. N. Lee: *Mater. Sci. Eng*., A206 (1996), 81.

27) H. N. Han, J. Lee, T. Yeo, Y. M. Won, K. Kim, K. H. Oh and J. Yoon: *ISIJ Int*., 39 (1999), 445.

28) H. Bester and K.W. Lange: Arch. Eisenhüttenwes., 43 (1972), 207

29) Y. Mimura: Master's Thesis, The University of British Columbia, Vancouver, (1989).

30) S. Chandra, J.K. Brimacombe, and I.V. Samarasekera: *Ironmaking Steelmaking*., 20 (1993), 104.

31) T. Shiraga, T. Mizoguchi, H. Esaka and S. Ogibayashi: *CAMP-ISIJ*, 7 (1994), 286.

32) K. Furumai, Y. Matsui, T. Murai and Y. Miki: *ISIJ Int*., 55 (2015), 2135.

33) E. Takeuchi, H. Fujii, T. Ohashi, H. Tanno, S. Takao, I. Furugaki and H. Kitamura: *Tetsu-to-Hagané*, 69 (1983), 1615.

34) Y. M. Won, T. Yeo, D. J. Seol and K. H. Oh: *Metall. Mater. Trans.B*., 31B (2000), 779.

35) D. Senk, S. Stratemeier, B. Bottger, K. Gohler and L. Steinbach: *Advanced Engineering Materials*., 12 (2010), 94.